Research Article | Vol. 26, No. 3 | 5 Feb 2018 | OPTICS EXPRESS 2435
Optics EXPRESS

Design of a compact CMOS-compatible photonic antenna by topological optimization

JULIÁN L. PITA,[1] IVAN ALDAYA,[2,3] PAULO DAINESE,[2] HUGO E. HERNANDEZ-FIGUEROA,[1] AND LUCAS H. GABRIELLI[1,*]

[1] *School of Electrical and Computer Engineering, University of Campinas (UNICAMP), 13083-852, Campinas, SP, Brazil*
[2] *Institute of Physics "Gleb Wataghin," University of Campinas (UNICAMP), 13083-859, Campinas, SP, Brazil*
[3] *Campus São João da Boa Vista, State University of São Paulo (UNESP), 13876-750, SP, Brazil*
[*] *lucashg@fee.unicamp.br*

Abstract: Photonic antennas are critical in applications such as spectroscopy, photovoltaics, optical communications, holography, and sensors. In most of those applications, metallic antennas have been employed due to their reduced sizes. Nevertheless, compact metallic antennas suffer from high dissipative loss, wavelength-dependent radiation pattern, and they are difficult to integrate with CMOS technology. All-dielectric antennas have been proposed to overcome those disadvantages because, in contrast to metallic ones, they are CMOS-compatible, easier to integrate with typical silicon waveguides, and they generally present a broader wavelength range of operation. These advantages are achieved, however, at the expense of larger footprints that prevent dense integration and their use in massive phased arrays. In order to overcome this drawback, we employ topological optimization to design an all-dielectric compact antenna with vertical emission over a broad wavelength range. The fabricated device has a footprint of 1.78 μm × 1.78 μm and shows a shift in the direction of its main radiation lobe of only 4° over wavelengths ranging from 1470 nm to 1550 nm and a coupling efficiency bandwidth broader than 150 nm.

OCIS codes: (130.3120) Integrated optics devices; (050.6624) Subwavelength structures; (200.2605) Free-space optical communication.

References and links

1. N. A. Hatab, C.-H. Hsueh, A. L. Gaddis, S. T. Retterer, J.-H. Li, G. Eres, Z. Zhang, and B. Gu, "Free-standing optical gold bowtie nanoantenna with variable gap size for enhanced Raman spectroscopy," Nano Lett. **10**, 4952–4955 (2010).
2. C. D'Andrea, J. Bochterle, A. Toma, C. Huck, F. Neubrech, E. Messina, B. Fazio, O. M. Maragò, E. D. Fabrizio, M. L. de La Chapelle, P. G. Gucciardi, and A. Pucci, "Optical nanoantennas for multiband surface-enhanced infrared and Raman spectroscopy," ACS Nano **7**, 3522–3531 (2013).
3. P. C. Wuytens, A. G. Skirtach, and R. Baets, "On-chip surface-enhanced Raman spectroscopy using nanosphere-lithography patterned antennas on silicon nitride waveguides," Opt. Express **25**, 12926–12934 (2017).
4. H. Huang, H. Li, W. Li, A. Wu, X. Chen, X. Zhu, Z. Sheng, S. Zou, X. Wang, and F. Gan, "High-efficiency vertical light emission through a compact silicon nanoantenna array," ACS Photonics **3**, 324–328 (2016).
5. A. Alù and N. Engheta, "Wireless at the nanoscale: Optical interconnects using matched nanoantennas," Phys. Rev. Lett. **104**, 213902 (2010).
6. G. N. Malheiros-Silveira, G. S. Wiederhecker, and H. E. Hernández-Figueroa, "Dielectric resonator antenna for applications in nanophotonics," Opt. Express **21**, 1234–1239 (2013).
7. J. L. Pita, I. Aldaya, O. J. S. Santana, L. E. E. de Araujo, P. Dainese, and L. H. Gabrielli, "Side-lobe level reduction in bio-inspired optical phased-array antennas," Opt. Express **25**, 30105–30114 (2017).
8. S. Pillai, K. R. Catchpole, T. Trupke, and M. A. Green, "Surface plasmon enhanced silicon solar cells," J. Appl. Phys. **101**, 093105 (2007).
9. K. R. Catchpole and A. Polman, "Plasmonic solar cells," Opt. Express **16**, 21793 (2008).
10. N. Liu, M. Tang, M. Hentschel, H. Giessen, and A. P. Alivisatos, "Nanoantenna-enhanced gas sensing in a single tailored nanofocus," in "Conference on Lasers and Electro-Optics," Optical Society of America (OSA, 2011), p. PDPC11.

#313870 https://doi.org/10.1364/OE.26.002435
Journal © 2018 Received 20 Nov 2017; revised 12 Jan 2018; accepted 15 Jan 2018; published 23 Jan 2018

Optics EXPRESS

11. J. C. Reed, H. Zhu, A. Y. Zhu, C. Li, and E. Cubukcu, "Graphene-enabled silver nanoantenna sensors," Nano Lett. **12**, 4090–4094 (2012).
12. J. Sun, E. Timurdogan, A. Yaacobi, E. S. Hosseini, and M. R. Watts, "Large-scale nanophotonic phased array," Nature **493**, 195–199 (2013).
13. P. Bharadwaj, B. Deutsch, and L. Novotny, "Optical antennas," Adv. Opt. Photon. **1**, 438 (2009).
14. A. E. Krasnok, A. E. Miroshnichenko, P. A. Belov, and Y. S. Kivshar, "All-dielectric optical nanoantennas," Opt. Express **20**, 20599 (2012).
15. G. N. Malheiros-Silveira, L. H. Gabrielli, C. J. Chang-Hasnain, and H. E. Hernandez-Figueroa, "Breakthroughs in photonics 2013: Advances in nanoantennas," IEEE Photon. J. **6**, 1–6 (2014).
16. P. Dumon, W. Bogaerts, D. V. Thourhout, D. Taillaert, R. Baets, J. Wouters, S. Beckx, and P. Jaenen, "Compact wavelength router based on a silicon-on-insulator arrayed waveguide grating pigtailed to a fiber array," Opt. Express **14**, 664 (2006).
17. A. Michaels and E. Yablonovitch, "Reinventing the circuit board with integrated optical interconnects," in "Conference on Lasers and Electro-Optics," Optical Society of America (OSA, 2016), pp. STu4G–2.
18. D. Taillaert, P. Bienstman, and R. Baets, "Compact efficient broadband grating coupler for silicon-on-insulator waveguides," Opt. Lett. **29**, 2749–2751 (2004).
19. A. Mekis, S. Gloeckner, G. Masini, A. Narasimha, T. Pinguet, S. Sahni, and P. De Dobbelaere, "A grating-coupler-enabled cmos photonics platform," IEEE J. Sel. Top. Quantum Electron. **17**, 597–608 (2011).
20. D. Taillaert, H. Chong, P. I. Borel, L. H. Frandsen, R. M. De La Rue, and R. Baets, "A compact two-dimensional grating coupler used as a polarization splitter," IEEE Photon.Tech. Lett. **15**, 1249–1251 (2003).
21. T. Yoshida, E. Omoda, Y. Atsumi, T. Nishi, S. Tajima, N. Miura, M. Mori, and Y. Sakakibara, "Vertically curved Si waveguide coupler with low loss and flat wavelength window," J. Lightw. Tech. **34**, 1567–1571 (2016).
22. B. Shen, P. Wang, R. Polson, and R. Menon, "An integrated-nanophotonics polarization beamsplitter with $2.4 \times 2.4 \mu m^2$ footprint," Nat. Photonics **9**, 378–382 (2015).
23. L. F. Frellsen, Y. Ding, O. Sigmund, and L. H. Frandsen, "Topology optimized mode multiplexing in silicon-on-insulator photonic wire waveguides," Opt. Express **24**, 16866 (2016).
24. A. Y. Piggott, J. Lu, T. M. Babinec, K. Lagoudakis, J. Petykiewicz, and J. Vuckovic, "Inverse design and implementation of a wavelength demultiplexing grating coupler," in "Conference on Lasers and Electro-Optics" Optical Society of America (OSA, 2015), pp. SM3I–2.
25. L. H. Frandsen, Y. Elesin, L. F. Frellsen, M. Mitrovic, Y. Ding, O. Sigmund, and K. Yvind, "Topology optimized mode conversion in a photonic crystal waveguide fabricated in silicon-on-insulator material," Opt. Express **22**, 8525 (2014).
26. E. Hassan, E. Wadbro, and M. Berggren, "Topology optimization of metallic antennas," IEEE Trans. Antennas Propag. **62**, 2488–2500 (2014).
27. R. Díaz de León-Zapata, G. González, E. Flores-García, A. G. Rodríguez, and F. J. González, "Evolutionary algorithm geometry optimization of optical antennas," Int. J. Antennas Propag. **2016**, 3156702 (2016).
28. J. L. Pita, P. C. Dainese, H. E. Hernandez-Figueroa, and L. H. Gabrielli, "Ultra-compact broadband dielectric antenna," in "Conference on Lasers and Electro-Optics" (Optical Society of America, 2016), pp. SM3G–7.
29. P. E. Gill, W. Murray, and M. A. Saunders, "SNOPT: An SQP algorithm for large-scale constrained optimization," SIAM Review **47**, 99–131 (2005).
30. L. Vivien and L. Pavesi, *Handbook of Silicon Photonics* (Taylor & Francis, 2016).

1. Introduction

Antennas operating at optical frequencies are becoming an essential part in applications from spectroscopy [1–3], communications [4–7], and photovoltaics [8, 9], to optical sensors [10, 11] and holography [12]. In addition, these antennas are expected to play a fundamental role in efficient photonic chip-to-chip communications, offering unprecedented bandwidth and power efficiency. Such broad application range has boosted research on photonic nano-antennas, which has led to a rich variety of implementations.

The first nano-antennas were made of metals, usually gold. These nano-antennas present a compact footprint because they support plasmonic resonances, but they suffer from high dissipative loss and challenging feeding mechanisms that result in poor radiation efficiency [13, 14]. Another drawback of metallic nano-antennas is that, owing to their resonant nature, their radiation pattern depends significantly on the wavelength and, consequently, they operate over a limited bandwidth. More recently, dielectric structures with controlled scattering patterns have been proposed as antennas, as they can be used as interfaces between guided and free-space waves. These devices have emerged as a solution to mitigate the high dissipative losses of plasmonic antennas [14, 15]. The easier integration within the well-established silicon-on-insulator (SOI)

Optics EXPRESS

platform, in combination with more efficient feeding and smaller wavelength dependence of the radiation pattern, makes this approach a more promising candidate for future high-performance broadband applications [12]. Usually, the improved efficiency and bandwidth is achieved, unfortunately, at the cost of a significant increase in footprint area.

Although for many applications the antenna size is not a critical factor, in multi-device chips, the antenna footprint may become the ultimate factor limiting the device density and can significantly increase the fabrication cost [16]. Another scenario where antenna size is crucial is in antenna arrays. Since performance and flexibility of antenna arrays improve as the number of elements increases, it is extremely important to use radiation elements with the smallest possible size (preferably smaller than half the operation wavelength). In regards to the direction of maximal radiation, if it does not occur vertically, the alignment between antennas may also pose a significant challenge, e.g. in interlayer coupling applications in a multilayer optical circuit board [17]. A dielectric antenna with broadside radiation pattern is then highly desirable.

Previous works have reported a Yagi-Uda antenna based on nano-spheres made of high-permittivity dielectric [14]. This Yagi-Uda antenna has a higher radiation efficiency than their metallic counterparts, but its radiation pattern still shows a strong dependence on the wavelength. Furthermore, this antenna is not easily fed and, consequently, it is unsuitable for photonic applications where the coupling of antennas to dielectric waveguides plays an important role. In addition, nano-spheres are difficult to fabricate and are not directly integrable within conventional SOI-platform.

The design of a compact CMOS-compatible antenna with high radiation efficiency and wavelength-independent radiation pattern remains as an unresolved challenge in integrated photonics. One candidate solution is the use of grating antennas, which has been proposed by several groups [18–20]. However, even if suitable for optical coupling, the large footprint of gratings renders them unfit for phased-arrays. A remarkable breakthrough in footprint reduction was made in [12], where a grating antenna with a size as small as $3\,\mu m \times 2.8\,\mu m$ was demonstrated, allowing the implementation of a 64×64 antenna array. However, these gratings are designed to present the direction of the maximum radiation in an angle greater than 20°. Non-vertical radiation increases the packaging complexity and cost dramatically in applications such as fiber-to-chip coupling [21]. Unfortunately, if the grating is designed to radiate vertically, the antenna efficiency drops sensibly since a great amount of intensity is reflected back toward the feeding waveguide.

More complex structures are then expected to be required to reduce backward reflection while keeping an almost broadside radiation pattern. In this context, topological optimization has emerged as a potential tool. It has already been employed in several photonic device designs to improve their figures of merit: in [22] a polarization beam splitter is designed using this technique, and in [23] and [24] the same approach is applied to find an optimal multiplexer design, whereas in [25] a mode converter is optimized. Topological optimization has also been used in the optimization of metallic antennas both at RF/microwave bands (1–10 GHz) [26], and at optical frequencies (500 THz) [27], but, to the best of our knowledge, it has not been used to aid in the design of all-dielectric photonic antennas. In this work, we extend our preliminary results presented in [28], where we use topological optimization to design a high-performance SOI-compatible dielectric antenna with a footprint of $1.78\,\mu m \times 1.78\,\mu m$ and an operating wavelength range exceeding 100 nm. Far-field measurements reveal that the optimized design results in an almost vertical emission from 1470 nm to 1550 nm, standing out as an excellent candidate for high data rate communications.

2. Design and simulation

The antenna design was performed in COMSOL Multiphysics through the in-built Sparse Nonlinear Optimization (SNOPT) algorithm, which starts from an unoptimized design (initial condition) and searches for an optimized design by minimizing a quadratic Lagrangian model [29]. After

Optics EXPRESS

each iteration, the resulting configuration is simulated using full-vector 3-d electromagnetic simulations, from which the value of the cost function is calculated. In order to find an optimized antenna topology, we considered a box having a 220 nm height and a base of 1.78 µm × 1.78 µm as the optimization region. The base of the region was divided in 112 × 112 square cells with 16 nm sides. Due to fabrication constrains, the silicon layer can present four heights within each cell: 0 (fully etched), 70 nm, 150 nm, or 220 nm. The optimization variables, then, are scalar quantities defined on each of those cells that indirectly relate to the thickness of the silicon layer in that cell. To be precise, the scalar value $0 \leq p_i \leq 4$ optimized for the i-th cell defines the refractive index of the 3 layers above the cell according to:

$$n_{ij} = n_{\text{clad}} + (n_{\text{core}} - n_{\text{clad}})u(p_i - j) \tag{1}$$

in which j equals 1, 2, and 3 for the lower (0 – 70 nm), middle (70 – 150 nm), and upper (150 – 220 nm) layers respectively, n_{clad} and n_{core} are the refractive indices of the cladding and core materials (silicon dioxide and silicon), and u is a smooth step function with 2 continuous derivatives [$x < -0.05 \Leftrightarrow u(x) = 0$ and $x > 0.05 \Leftrightarrow u(x) = 1$]. The goal function, or the figure of merit of the device, was defined as the sum of the far-field intensities in five different directions, shown in Fig. 1(a), for a constant input power in the simulation. These directions correspond to a 20° angle around the perpendicular to the substrate.

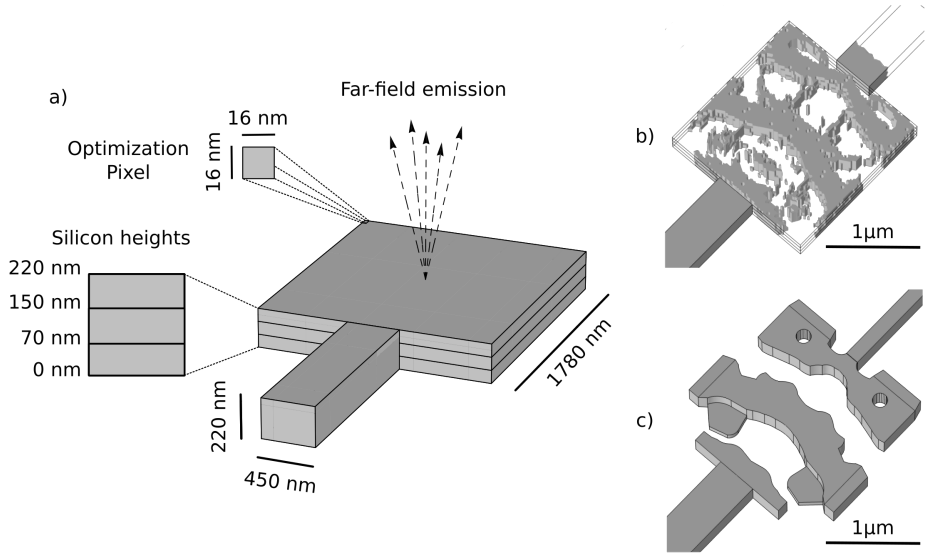

Fig. 1. Design of the optimized antenna. (a) Optimization region indicating the pixel size, the four possible silicon layer heights, the dimension of the feeding waveguide, and the far-field radiation directions that are used in computing the figure of merit of the antenna. (b) Optimized design after 78 iterations. (c) Smoothed design suitable for fabrication.

The time to simulate each configuration and total optimization time were reduced by taking advantage of the problem symmetry, which allows the reduction of optimization variables and the simulation of only half of the domain. The outcome of the optimization algorithm after 78 iterations (requiring 39 hours in a computer with 128 GB RAM and a processing speed of 1.25 TFlops) is shown in Fig. 1(b). At this stage, the optimized structure presents a significant number of small isolated silicon regions and sharp angles that do not meet fabrication constrains.

In order to overcome this issue, the structure was spatially filtered to remove the small features and sharp angles, resulting in the smoothed design shown in Fig. 1(c). This filtering does not

Optics EXPRESS

significantly affect the radiation pattern of the designed device according to simulations. There are two remarkable points to note: first, the different layer heights break the vertical symmetry of the structure, favoring the radiation in the upward direction; second, the presence of an output waveguide (which is thinned out in the smoothed design) reduces the reflected light back to the feeding waveguide and, in addition, can be used for power monitoring.

Before fabrication, the performance of the antenna was tested through 3-d FDTD simulations performed in Lumerical, which allows efficient calculation of the transfer function over a broad wavelength range. Figure 2(a) shows the upward (η_u) and downward (η_d) emission efficiencies, as well as the reflection (R) and transmission (T) coefficients, revealing a broad 1-dB bandwidth exceeding 100 nm. According to simulation results, the maximum emission efficiency reaches 80% at 1466 nm, being 50% of the input power radiated upward and the remaining 30% downward (which could contribute to the forward emission after proper reflection in the silicon substrate). At 1550 nm, the upward and downward emission efficiencies drop down to 38% and 28%, respectively, resulting in a total radiation efficiency of 66%. It is worth noting that the asymmetry between upward and backward emitted powers is maintained over the whole bandwidth, decreasing only at the longer wavelengths. With regards to reflection and transmission, the former reaches a minimum of 13% at 1480 nm, whereas the latter does not exceed 9.6% in the analyzed wavelength range.

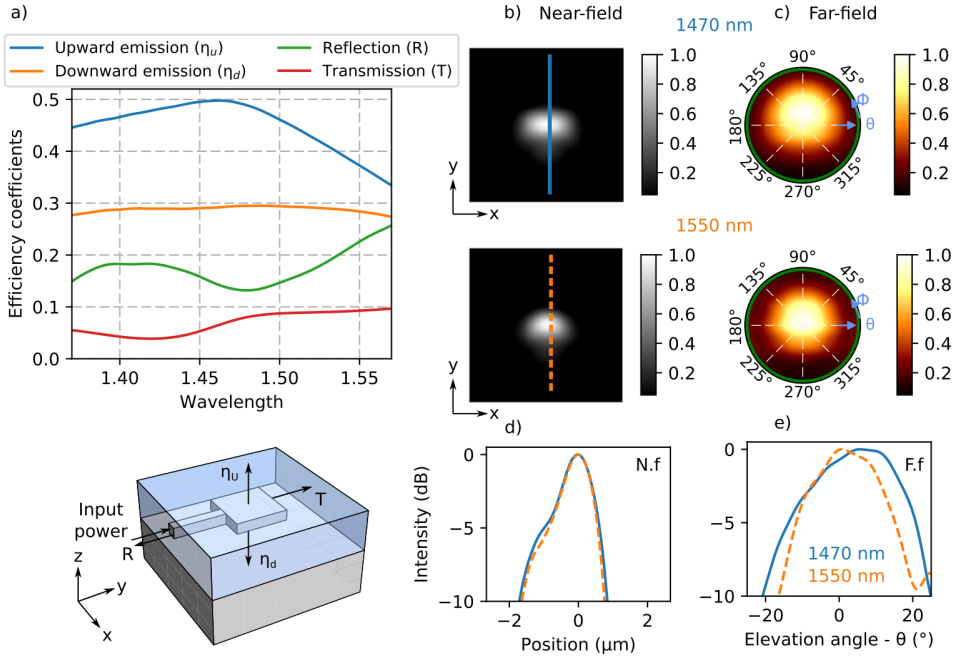

Fig. 2. Simulation of the optimized antenna at wavelengths from 1400 nm to 1550 nm. (a) Transmission and reflection coefficients, as well as emission efficiencies in the upward and downward directions. (b) Near-field intensity profiles and (c) far-field radiation patterns at 1470 nm and 1550 nm. (d) Cuts of the near-fields (b) along the indicated paths. (e) Cuts of the far-fileds (d) along the 90° azimuthal angle. N.f and F.f. stand for near-field and far-field, respectively.

The radiation properties of the designed antenna are illustrated at two wavelengths: 1470 nm and 1550 nm. Figure 2(b) and 2(c) show the near-field intensity profiles and the far-field radiation patterns of the optimized antenna, respectively. We point out that in this text we use the terminology commonly adopted in the characterization of optical antennas, where near-field and

Optics EXPRESS

far-field measurements represent, respectively, the real-space and k-space images of the source (reactive components and radiative components outside the numerical aperture of the lens are not captured in these measurements). As can be seen, the near-field profile presents a single main spot. This point is easier to appreciate in Fig. 2(d), where the near-field profiles in the directions indicated in Fig. 2(b) are represented. Comparing the profiles in Fig. 2(b) [or Fig. 2(d)] we can see a minimal change in the near-field pattern between the two wavelengths, which agrees with the broad bandwidth shown in Fig. 2(a). This behavior in the near-field profile already indicates that the far-field radiation pattern will also maintain its configuration in the same wavelength range. Confirming that expectation, the radiation patterns in Figs. 2(c) and 2(e), obtained through a near-field-to-far-field transformation, differ only slightly and present two remarkable features: first, the lack of secondary lobes within a cone of 24° (corresponding to the numerical aperture of the lens employed later in the experimental characterization); second, a minimal shift in the direction of the main lobe [better appreciated in cuts at $\phi = 90°$ in Fig. 2(e)]. The former attribute is critical to improve efficiency and security in communication channels, whereas the latter is desirable as it leads to a wavelength-independent alignment between transmitter and receiver (e.g. chip and fiber in case of fiber-to-chip coupling).

3. Fabrication and characterization

The optimized antenna was fabricated at imec/Europractice using optical lithography on an SOI platform with 2 µm of buried silicon dioxide and a silicon dioxide cladding approximately 1.5 µm thick. As mentioned, this fabrication process implied several constrains that were taken into account during the design process. In Fig. 3(a), a scanning electron microscope (SEM) image of the fabricated device is displayed, revealing a high degree of similarity with the optimized design. As designed, the device has a footprint as small as 1.78 µm × 1.78 µm, i.e., 60% smaller than the grating antenna from [12].

Figures 3(b) and 3(c) show the setups employed to characterize the fabricated antenna in near-field and far-field respectively. The tunable laser source (TLS) is followed by a polarization controller (PC) to rotate the state of polarization before coupling into the SOI chip via a lensed fiber (LF) and an inverted taper fabricated on the chip. The alignment between the chip and the feeding fiber, as well as between the chip and the lens system, is optimized and maintained by means of two piezo-electric stages (PSs). In order to measure the near-field profiles we built a $4f$-system based on a Mitutoyo Plan-Apo NIR infinity corrected objective L_1 (NA 0.4) and a second infinity corrected tube lens L_2, as shown in Fig. 3(b). The far-field radiation pattern was measured using the $2f$-system presented in Fig. 3(c), which is derived from the $4f$-system by removing lens L_2. Both the near-field profiles and the far-field radiation patterns were captured using a short wave infrared (SWIR) InGaAs CCD camera. It is worth noting that, given the small footprint of the analyzed antenna, this setup allows the accurate measurement of both near and far-field intensities.

The obtained images are shown in Figs. 3(d) and 3(e), whereas the cuts in the indicated directions are presented in Figs. 3(e) and 3(f). In order to reduce the effects of pixelation and noise in Figs. 3(e) and 3(f), the camera images were processed using a 2nd order Savitzky-Golay filter. In regards to the near-field profiles, they are similar in size to those obtained through simulation. Comparing the measured and simulated profiles in the selected direction, that is Figs. 2(d) and 3(f), a reasonable agreement is observed. The measured far-field radiation patterns shown in Fig. 3(e) are also similar to those obtained by simulation and presented in Fig. 2(c). The far-field measurements, however, suffer from an interference pattern that can be attributed to stray reflections in the optical systems or at the bottom of the silicon substrate [12]. This effect persists in Fig. 3(g), giving rise to a small ripple in the plots. Nonetheless, experimental results reveal that two of the most important features of the antenna are confirmed: on the one hand, the direction of maximum radiation is almost orthogonal to the substrate plane (less than 4° elevation) and, on

Optics EXPRESS

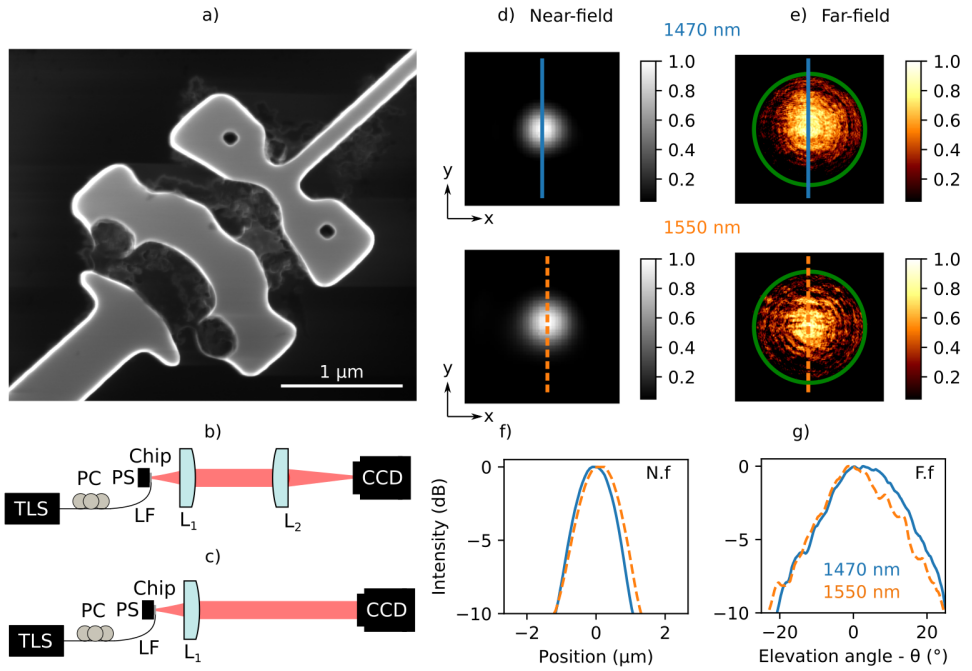

Fig. 3. Characterization of the fabricated antenna at 1470 nm and 1550 nm. (a) SEM image of the antenna under test. (b) Experimental setups for measurements of near-field profile and (c) far-field radiation pattern. TLS: tunable laser source; PC: polarization controller; LF: lensed fiber, L_1: Microscope objective; L_2: lens; CCD: InGaAs coupled charge device camera. (d) Captured near-field profiles and (e) far-field radiation patterns. (f, g) Cuts of the near-fields (d) and far-fields (e) along the indicated paths, respectively. N.f. indicates near-field, while F.f represents far-field.

the other, the far field radiation pattern maintains its shape over a wavelength range of 80 nm.

Finally, we evaluate the antenna as a chip-to-fiber coupler and its dependence on the wavelength. In order to get the coupling efficiency over the range spanning from 1350 nm to 1650 nm, we use an optical spectrum analyzer OSA equipped with a superluminiscent light emitting diode (SLED), as shown in Fig. 4(a). The output of the SLED is first passed through a linear polarizer (LP), after which a polarization controller (PC) is employed to optimize the polarization matching with the quasi-TE mode in the feeding waveguide. It is worth noting that since the light is coupled into the chip using an inverted taper, the input coupling is virtually independent of the wavelength for the analyzed range. The light radiated by the antenna is then captured by a second lensed fiber and the output is monitored on the OSA, which has been configured to remove the SLED baseline. The obtained coupling efficiency is presented in Fig. 4(b), revealing a 3-dB bandwidth exceeding 150 nm, which is significantly broader that 60 nm typical in surface couplers [30].

4. Conclusions

In this paper we report on the design, fabrication, and characterization of an SOI-compatible ultra-compact nanophotonic antenna with broadside radiation pattern. A footprint as small as 1.78 µm × 1.78 µm is achieved by means of topological optimization over four different silicon layers. For wavelengths ranging from 1470 nm to 1550 nm, numerical simulations show a virtually wavelength-independent near-field profile, leading to a far-field radiation pattern

Optics EXPRESS

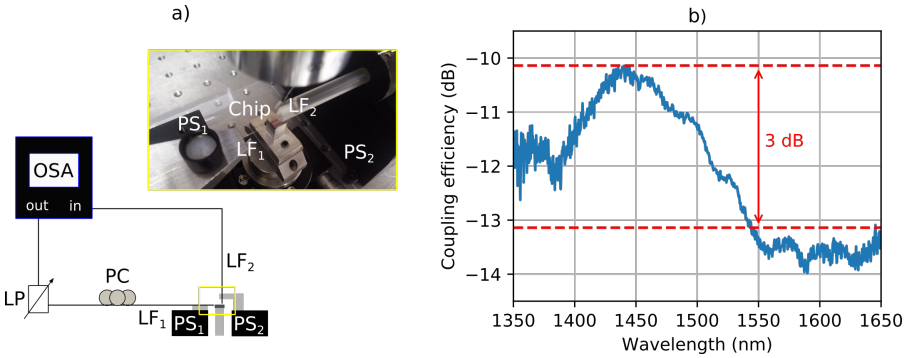

Fig. 4. Antennas for coupling. (a) Experimental setup employed to measure the antenna bandwidth. OSA: optical spectrum analyzer; LP: linear polarizer; PC: polarization controller; LF: lensed fiber; and PS: piezo-stage. (b) Measured coupling efficiency.

with a shift of only 4° from broadside. Experimental characterization reveals that the fabricated antenna preserves the main desired features, i.e. broadside radiation and wide range of operating wavelengths. The reduced size of the optimized antenna alongside its radiation properties and coupling bandwidth make this design a promising candidate for several applications, such as intra-chip communications, light coupling to multi-core fibers, and implementation of large phased antenna arrays.

Funding

National Council for the Improvement of Higher Education (CAPES); the State of São Paulo Research Foundation (FAPESP) (2008/57857-2, 2013/20180-3, 2015/04113-0, 2015/24517-8, and 2016/19270-6); National Council for Scientific and Technological Development (CNPq) (574017/2008-9, 465757/2014-6, 446746/2014-2, and 312110/2016-2).

Acknowledgments

The authors thank M. S. Faria for assisting with the high-performance computation.